NIRC-2

The Keck Near-Infrared AO Camera

Pre-ship testing.

March 02 - April 17, 2001

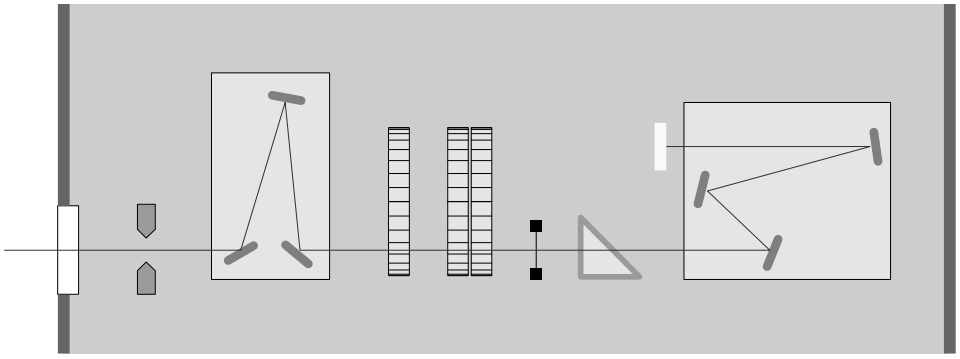

Prepared by:
David Thompson, Eiichi Egami, Marcin Sawicki
California Institute of Technology

Table of Contents

1 Introduction

This report details testing of the NIRC-2 AO Camera at Caltech over the March 02 - April 17, 2001 period encompassing the time immediately prior to the pre-ship review, scheduled for April 23, 2001. Our testing at Caltech primarily encompassed the basic characterization of the instrument, from the performance of the array, optics and electronincs, to calibration of the mechanisms inside the dewar. There is some overlap with testing by the CARA software group and the UCLA electronics group.

2 Cosmetics

2.1 Cracks

The InSb material from which the Aladin detector is made is a crystalline solid with reasonably strong cleavage planes. This means that stresses, such as thermal cycling or mechanical stress, can cause the InSb crystal to fracture, or existing fractures to propagate.

The science-grade array (C211) was installed in NIRC2 on January 20, 2001. It has a single crack (Figure 1) in the lower left quadrant (Q4) which starts at the edge of the array and ends at pixel (214,361).

The array has undergone a single warmup-cooldown cycle since originally cooled after installation. Images obtained before and after this thermal cycling show that the crack has not propagated or changed in any way.

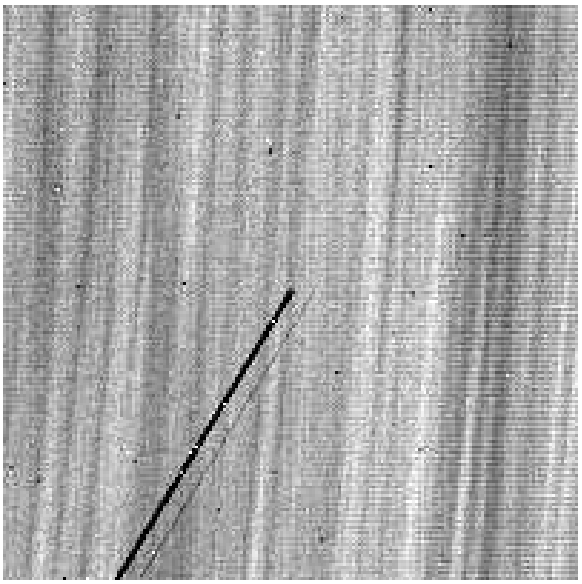

Figure 1: The end of the crack in the C211 array. The image is only 201×201 pixels and does not extend down to the lower left corner of the array. This image is not flatfielded. There is an electronic ghost of the crack visible offset 8 columns to the left.

2.2 Uniformity

The relative response of the C211 array is good, with the exception of four regions with depressed sensitivity (Figure 2). Their placement around the edge of the array should minimize their impact on science observations. Normal flatfielding techniques will remove them satisfactorily. The largest and least sensitive depression, by the lower left edge, has a minimum reponse of ∼73% of the mean, while the others range from 86% to 93% of the mean.

There are also curved striae aligned roughly vertical on the array, ranging up to a few tens of pixels in width, visible in Figure 2. These striae have an rms amplitude of 1% around the local mean. Normal flatfielding techniques will also remove them satisfactorily.

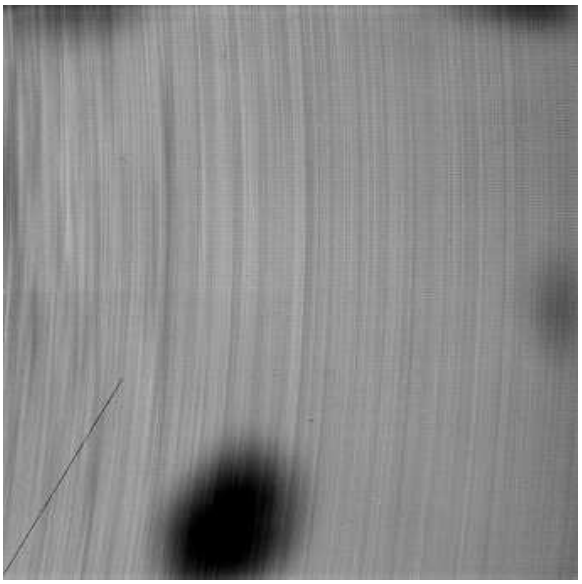

Figure 2: The relative response of the C211 array. The full array is shown.

A histogram of the relative reponse is shown in Figure 3. The FWHM for the peak is 0.054, while the long tail to 0.73 is from the four regions with depressed sensitivity.

2.3 Bad Pixels

There are no absolutely dead pixels (zero response) on the C211 array. Even the crack shows some response, typically in the 60-70% range. The number of hot pixels (high dark current) really depends on what type of data you are tak-

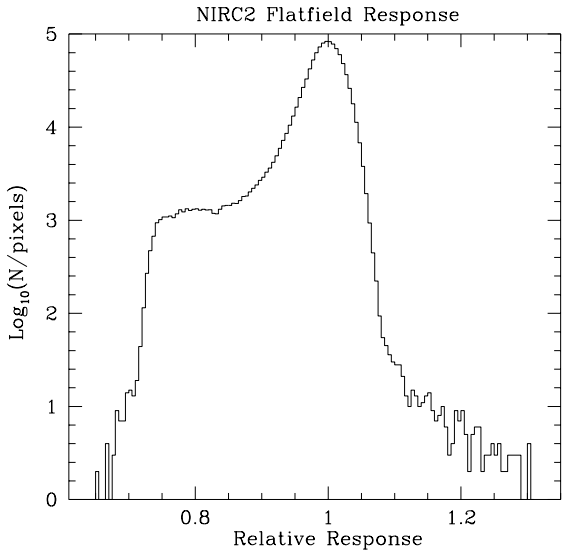

Figure 3: A histogram of the relative response of the C211 array. The tail of the distribution to ∼0.7 comes from the areas of depressed sensitivity around the edge of the array.

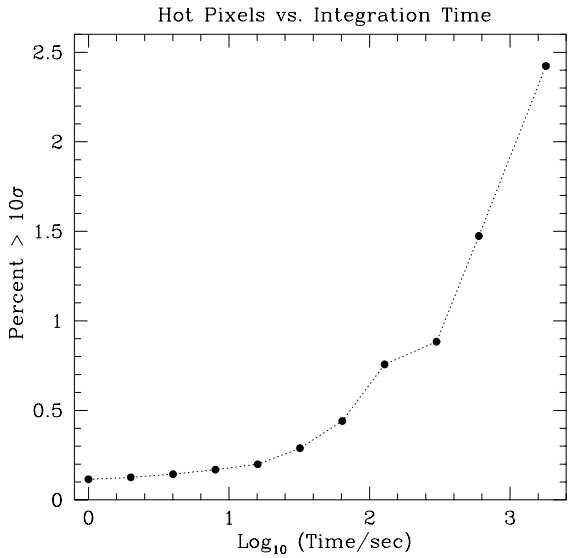

Figure 4: The percent of pixels exceeding 10σ as a function of integration time.

ing (high background imaging or low background spectroscopy) as well as how long of an exposure you are doing. In order to quantify this at some level, we plot the fraction of pixels which exceed ten times the 1σ dispersion of the entire array as a function of the exposure time in Figure 4.

For short exposures, only about 1000 pixels (∼0.1%) are hot. Even for long exposures (the longest tested was 1800 seconds), less than 2.5% of the pixels exceed the mean level by more than 10σ. It is important, however, to keep in mind that these are not necessarily unrecoverably bad pixels! As long as they are not saturated in the exposure time used (from dark current and real signal), pixels with a high but stable dark current should subtract out just fine.

Note that the distribution of hot pixels is not uniform on the array. The top half of the array (quadrants 1 and 2) show a higher density (about a factor of two) of hot pixels on long exposures than the lower half of the array. This can be seen Figure 5, which plots the average of all 1024 columns as a function of the row number.

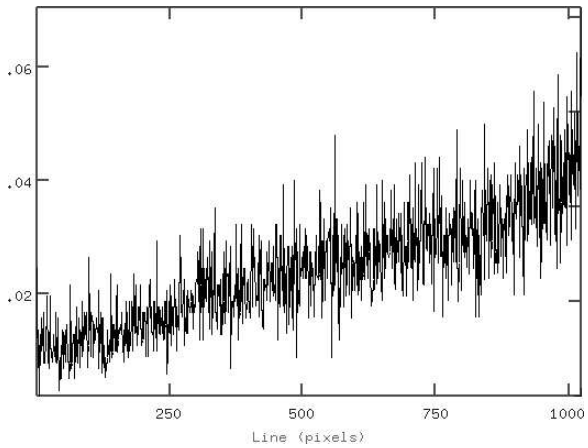

Figure 5: Distribution of hot pixels ($> 10\sigma$) on an 1800 s dark exposure.

Tests performed by D. Thompson.

3 Quantum Efficiency

Tests in progress.

Tests performed by d. thompson.

4 Read Noise

We determined the read noise as a function of the number of reads (N) used in multiple correlated sampling (MCS), or Fowler sampling. The tests were done at the default sample rate (250 kpix/s) on the full array. We used an 80 second *dark* exposure for all images, with no light reaching the array. This is close to the minimum possible exposure time when using 512 samples for both the initial and final reads in MCS (about 73 seconds). We obtained four sets of data consisting of pairs of images at 17 different settings for N spanning the range of one (double-correlated sampling) to 512.

The pairs of images were differenced and residual constant offsets between quadrants were removed before averaging the 4 images. The source of these constant offsets between the quadrants is not known, and does not show up in single read exposures or DCS data. Figure 6 plots the log of the root-mean-square noise per pixel in DN (corrected for the averaging) vs. log(N).

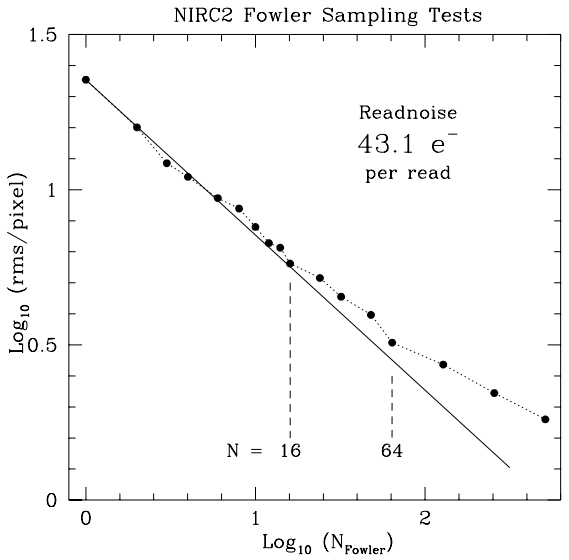

Figure 6: Read noise as a function of the number of Fowler samples.

A perfect detector would show a slope of -0.5 (shown by the solid line in Figure 6), indicating that the noise goes down as the square root of N for small N. The measured points (filled circles) follow this relation well up to N=16, and show only minor deviations up to N=64.

A fit to the data between N=1 and N=16 gives an intercept of 21.787 DN. This is the combined readnoise from two images each of which has an initial and a final read. Thus, four reads contribute to the noise at log(N)=0, and we must reduce the 21.787 DN by a factor of the square-root of 4. To convert to electrons, we must also multiply by the gain, which is 4.0 e^-/DN. This gives a readnoise in electrons for a single read of the array of 43.1 e^-.

We note that the array continues to show a significant reduction in the read noise all the way up to N=512, even if it does not drop as rapidly as root-N. This implies that for long exposures under low background conditions (e.g. high-resolution spectroscopy in the *J* band), it is advantageous to use Fowler sampling with a large N to reduce the read noise as much as possible. With a large number of reads, there is a noticeable glow in the corners of the array. This should have little impact on science observations because it is small enough to minimally increase the noise.

There is one source of uncertainty in these measurements coming from pickup noise. The source of the pickup noise was not determined at the time of these tests. We attempted to minimize problems from pickup noise by obtaining four sets of data and averaging them. This is also less of a problem at higher N, since any pickup noise appears to be uncorrelated from one read to the next. Therefore, we do not think that this is a major problem in these measurements.

One other *feature* was noticed during testing of the NIRC2 array. Occasionally a dark hole, apparently known as *Fowler Holes*, would appear in an image. These features are always negative, and are not randomly distributed across the array (they are far more frequent in the right half of the array, quadrants 1 and 3). Figure 7 plots the positions on the array for the 29 holes. Note that 27 are unique; two may be memory effects from the strongest hole in the Fowler testing data, which consists of 126 images.

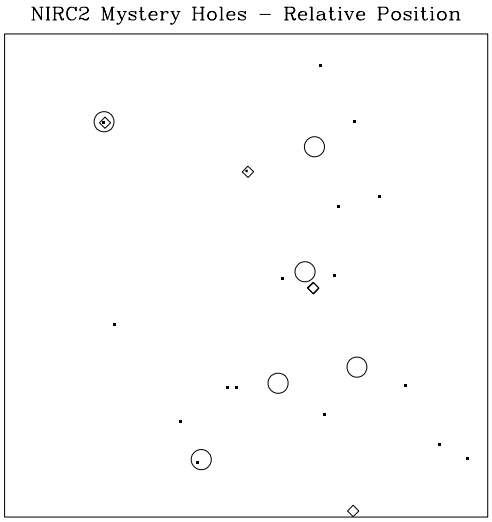

Figure 7: Distribution of the holes appearing on the detector. The size of the symbol reflects the strength of the hole (strong, medium, or weak).

The Fowler holes appear very uniform in size, roughly 40 pixels diameter. They are uniformly circular, and vary in strength. The *darkest* holes show a deficit of about 150–200 DN peak depth, while the weakest are only faintly visible in the images. When they appear in MCS data with large N, the noise is low enough to see a fainter positive ring around the stronger holes. We show images of the six stronger holes in Figure 8. The source of these holes is currently unknown.

The data obtained for measuring the array dark current includes ten DCS exposures with an integration time of 1801 seconds. This is a total integration time somewhat larger than the total integration time summed over all 126 images obtained in the Fowler sampling tests. They were also inspected for these holes, and we found a total of only 6 unique holes. This differs from the Fowler sampling data at about the 3 sigma level.

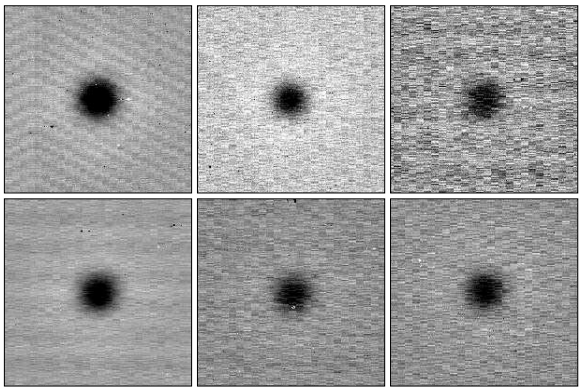

Figure 8: Images of six of the stronger holes. They tend to be roughly the same size, about 40 pixels in diameter, independent of the strength. In several of the images, you can see a faint halo around the hole. Each subimage is 201 pixels square.

Tests performed by D. Thompson.

5 Dark Current

The InSb detector has a small current even in the dark, It is indistinguishable from a current generated by astronomical sources, so care must be taken to correct for this dark current. For long exposures, such as during spectroscopic observations, the dark current can be significant.

NIRC2 was configured with the shutter closed and with crossed filters to ensure that no light reached the array. We then obtained 10 sets of data at exposure times of 1801+1, 601+1, 301+1, and 61+1 seconds in single-correlated read mode. The data were obtained overnight with a script, and the long exposures were done first to allow the array to settle into a stable state. The array had also been sitting with the shutter closed for a day or two prior to these tests while testing the array's readnoise.

The image pairs were differenced, and the resulting 10 images in each set averaged with sigma-clipping to remove cosmic rays. The averaged images were then divided by the exposure time and multiplied by 5 (but see note below), the nominal gain (electrons per data number) of the NIRC2 electronics. This yielded images with pixel values equal to the dark current in electrons per second per pixel.

Figure 9 shows the histograms for the four images, and Table 5 lists the value of the peak of each histogram. There is a systematic offset, such that lower exposure times give larger dark currents. Note that the width of the distributions is a function of the constant read noise divided by the different exposure times.

Dark current vs. Exposure Time

Exp. Time (seconds)	Dark Current (e^-/s/pixel)
60	0.558
300	0.159
600	0.112
1800	0.064

There is an apparent decrease in the dark current with increasing exposure times. The source of this effect is not known at this time. For long exposures ($t > 600$ s), the mean dark current is around 0.1 e^- per second.

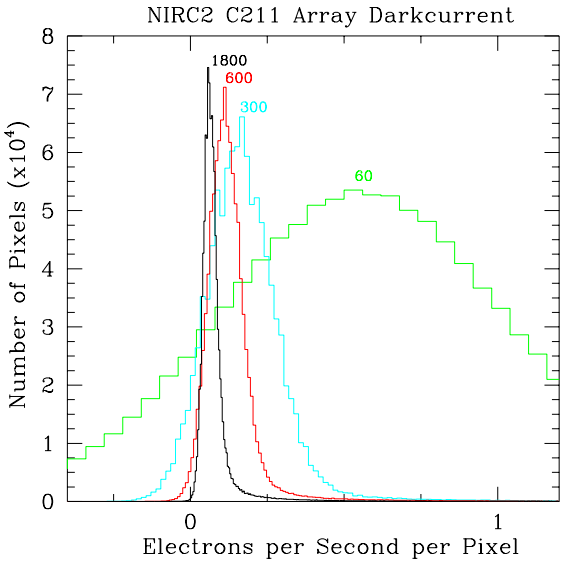

Figure 9: Dark currents for the science detector in NIRC2 measured at 1800, 600, 300, and 60 seconds. The values for the peaks of each histogram are given in Table 5.

Tests performed by D. Thompson.

6 Memory

The InSb array shows some memory of prior images taken. The mechanism responsible for this effect is not known. There appears to be some memory even of relatviely low light levels (well below saturation) which can persist for several minutes. Memory effects from heavy oversaturation of the array have been seen up to 24 hours after the exposure occurred.

Because NIRC2, as with most infrared instruments, does not have a fast shutter used to time exposures, the array sees light whenever the slow shutter is open. Care must be taken by the observers to control the light reaching the array, to avoid saturation. Further work is necessary, as well, to better understand the source of this memory effect and work on methods to mitigate its impact on science observations.

We conducted preliminary testing of the image memory for NIRC2 in order to demonstrate and quantify this effect. Two tests were done: the first looked at the decay rate with time, while the second looked at flushing the array with multiple reads prior to an exposure. This flushing of the array is currently used (with success?) by NIRSPEC prior to long spectroscopic exposures.

6.1 Decay Rate

NIRC2 was configured for wide-field K-band imaging, with the slit mask placed in the focal plane. This produces seven slit images across the array. Images were obtained with the shutter closed to verify that the array was clean, i.e. no memory signals from prior exposures.

Using a script so that successive commands were executed rapidly, NIRC2 was requested to open the shutter, sleep for 30 seconds, close the shutter, then begin a series of 60 second exposures. No images were taken during the 30 second period when the shutter was open, but light from the seven slits was reaching the array. Note that when not in the process of taking an exposure, the NIRC2 electronics go into a continuous reset state. This presumably continuously wipes the array of any incoming signal.

However, as we can see in the results from this test, a memory signal is still present. Figure 10 shows a slice of the first twelve 60-second images obtained after closing the shutter. The narrowest slit is on the left. While the memory signal does decrease over time, it is still present in the last image, obtained about 12 minutes after closing the shutter.

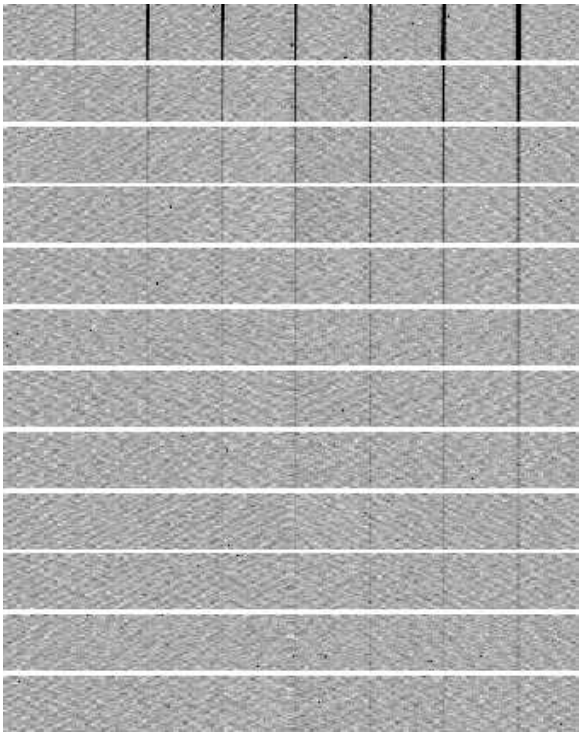

Figure 10: Images of the seven slits. Time increases from top to bottom, with the first image taken immediately after closing the shutter. Each image is ~68 s (60 s exposure plus overhead).

A second run with the same script was made, but the first exposure after the shutter closed was replaced by a 60 second sleep command. This was to check if the memory image would decay even if no reads were done. We extracted the peak value in each of the slit images for both runs, shown in Figure 11. The data are plotted relative to the images taken starting ~60 seconds after the shutter closed. We applied a one-minute shift to the second set of data, corresponding to the 60 second sleep prior to the series of images being taken. The decay rate is

consistent with a $t^{-1\pm0.2}$ decay rate.

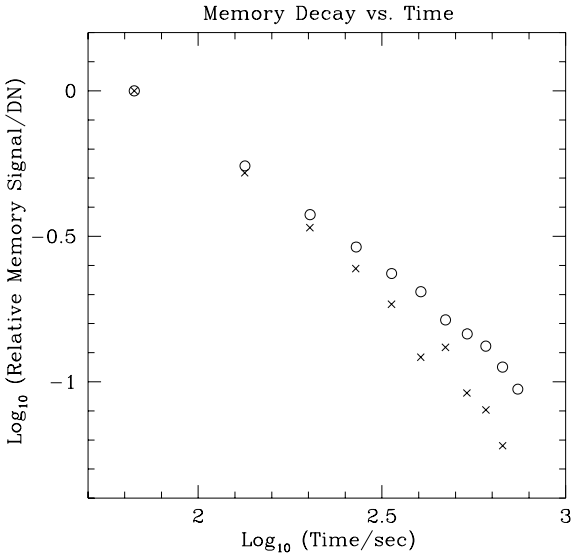

Figure 11: Plot of the memory signal vs. time since closing the shutter. The decay is roughly proportional to $t^{-1\pm0.2}$.

6.2 Multi-Read Flush

Memory problems have apparently been encountered with the NIRSPEC array as well. The current procedure there is to perform a multi-read flush of the array prior to starting long spectroscopic exposures. This flush takes the form of 50 coadded images of 0.25 second duration in DCS mode (so 50 resets and 100 reads are done). We set up a script to test this which has the form:
1) flush 50×0.25 s
2) take reference 60 s image
3) open shutter for 30 seconds
4) flush NN $\times$ 0.25 s
5) sleep to compensate varying NN
6) take test image.

with NN equal to 0, 1, 2, 4, 8, 16, 32, and 64. The length of the sleep (step 5) varied so that steps 4+5 took a constant amount of time. This should eliminate variations in the memory level which are due to decay with time.

For each pair, we subtracted the reference image from the test image. The results are shown in Figure 12. Aside from the NN=0 test, there is no difference in the level of the memory signal. This would indicate that the multi-read flush is *not* effective in reducing or eliminating the memory signal.

Figure 12: Images of the seven slits. NN, the number of coadded 0.25 s DCS reads used to flush the memory signal, is zero for the top image, then 1, 2, 4, 8, 16, 32, and 64, increasing to the bottom image. Note that the memory signal *does not decrease* with increasing NN.

Tests performed by D. Thompson.

7 Linearity

Tests in progress.

Tests performed by d. thompson.

8 Slit Angle

The purpose of this test is to determine the alignment of pixel columns on the array with the focal plane masks. Because of the way the focal-plane slider (SLS) is made, we assume that the slits are parallel to the aperture, focus, and distortion masks, and measure only the slits - the most critical component in the focal plane. These tests were done in imaging mode, with no grism in the light path. The use of a grism (spectroscopic mode) will introduce some additional aberrations, which are detailed in the section on grisms and spectroscopy.

Prior to warming NIRC-2 on February 17, 2001, we measured the angle of the slits on the WIDE camera to be 4 pixels from end to end. In fitting the slit image centroid as a function of the row on the array, we also found that there is some curvature to the slit image which is well-fit by a quadratic polynomial. This can be seen in the figures below.

While NIRC-2 was warm, the array was rotated in its mount to compensate for this slit angle. However, subsequent testing (Figure 13) has shown that the array moved little, if any. It is possible that the attempted rotation was elastic and the array returned to its original orientation. As it currently stands, the slits are slightly rotated with respect to columns on the array, detailed below. However, for all three cameras, there is a significant span (several hundred pixels) on the array where the slit is essentially aligned with the array columns to better than one pixel.

For the WIDE camera (Figure 13), the end-to-end deviation in the slit image is ∼3.5 pixels or 0.″2, while the *maximum* deviation is ∼4.5 pixels over 680 pixels or 0.″38. A zero slope, where the slit image is perfectly aligned with the columns on the array, occurs at row 680. There is less than one pixel deviation from this position over ±300 pixels.

The MEDIUM camera (Figure 14) is very similar to the WIDE camera. The end-to-end deviation in the slit image is ∼3.5 pixels or 0.″2, while the *maximum* deviation is ∼4.5 pixels over 620 pixels or 0.″42. The zero slope occurs at row 620.

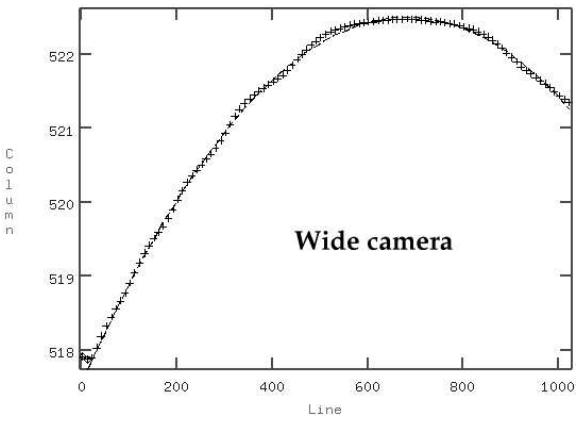

Figure 13: Slit centroid (Column) on the WIDE camera as a function of the row (Line) number.

There is less than one pixel deviation from this position over ±300 pixels.

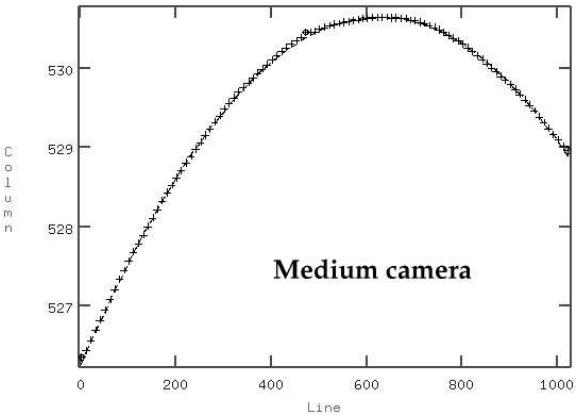

Figure 14: Slit centroid (Column) on the MEDIUM camera as a function of the row (Line) number.

The NARROW camera (Figure 15) differs from the other two. Here, the end-to-end deviation in the slit image is only ∼1.7 pixels or 0.″1, while the *maximum* deviation is ∼2.6 pixels over 644 pixels or 0.″23. The zero slope occurs at row 380. There is less than one pixel deviation from this position over ±380 pixels.

TESTS PERFORMED BY D. THOMPSON.

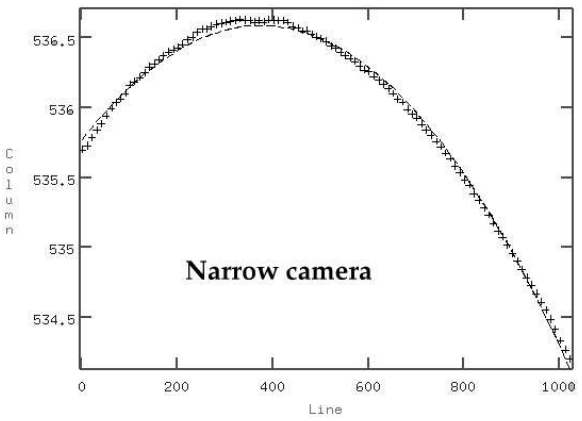

Figure 15: Slit centroid (Column) on the NARROW camera as a function of the row (Line) number.

9 Focus[1]

Purpose: The focal plane formed by the spectrograph should be flat in an ideal case, but in practice there are deviations introduced by the imperfection of the optics. The purpose of this test is to detect such deviations. This is done by measuring the focal length variation as a function of position on the detector.

Focus Mask: The focus mask used for this test is a flat plate with 20 columns of 8μm diameter holes with 7 mm spacing. This mask is placed in the slit selector with some tilt such that each column of the holes is at a different distances from the detector (150 μm between two columns). By design, the perfect focus should be achieved for the holes at the position of column 9.5. By sliding this mask over the detector and examine the change of image shape at various detector positions, it is possible to determine how the optimal distance between the slit selector and the detector change from position to position.

Procedure: The test was performed in the following way:

1. The left edge of the focus mask was placed near the right edge of the detector (i.e., lower slsraw counts).
2. The focus mask was moved to the left by half of the spot spacing (1382/2 = 691 counts), and an M_s-band image was taken.
3. This procedure was repeated until the right edge of the focus mask comes near the left edge of the detector.

The images 1, 3, 5,... were subtracted from the images 2, 4, 6,... to remove the background illumination pattern. By tracing the spot size variation from image to image at the same position on the detector, the best focus can be determined for that position. The above procedure will produce a rectangular grid pattern of x××x, 18×17, and 38×36 spots for the narrow, medium and wide camera, respectively, after the points near the edges were discarded.

For each grid point, the spot size was measured for 18 different focus values. The two most extremes values (column 1 and 20 on the focus mask) were discarded from the analysis. The spot size was determined by fitting a a 2-D elliptical gaussian and calculating,

$$\sqrt{\text{FWHM(major axis)}^2 + \text{FWHM(minor axis)}^2}.$$

The optimal focus value for each grid point was determined by fitting a second-order polynomial to the 18 measurements and find its minimum.

[1]Caution: These data were taken with the old camera positions. The testing with the new camera positions is in progress.

9.1 Narrow Camera

Among the three cameras, the Narrow camera shows the smallest variation of the focal length as a function of position on the detector, but the variation is non-negligible. The best focus column changes from 6 near the edges to 10 at the center, corresponding to the focal length difference of 600 μm. The foucs change is relatively smooth and circularly symmetric with the center of symmetry close to the field center.

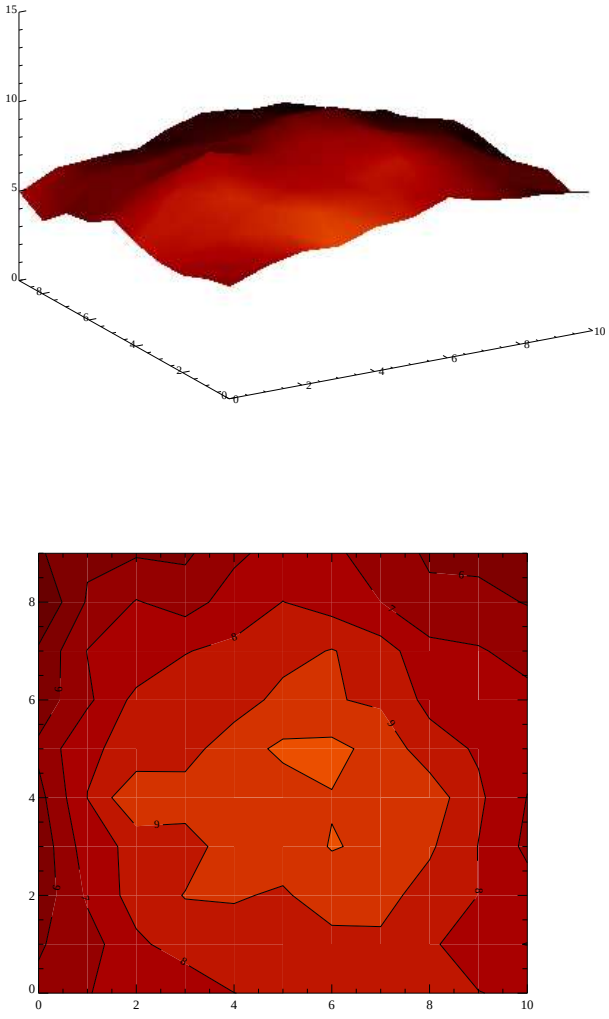

Figure 16: Narrow Camera — Upper: The focal length variation shown as a 3-D surface map. The z-axis indicates the number of the column on the focus mask which produces the best focus. The detector area was sampled by a 11 × 10 spots; Lower: The contour map constructed from the upper 3-D map. No smoothing was applied.

9.2 Medium Camera

The medium camera shows the most severe curvature with the focal plane. Figure 17 shows that the optimal focus value is 14–15 near the field center while it is 7–8 near the edges, corresponding to the focal length difference of 1.05 mm. The focus change is again smooth and nearly circularly symmetric with the center of symmetry close to the field center.

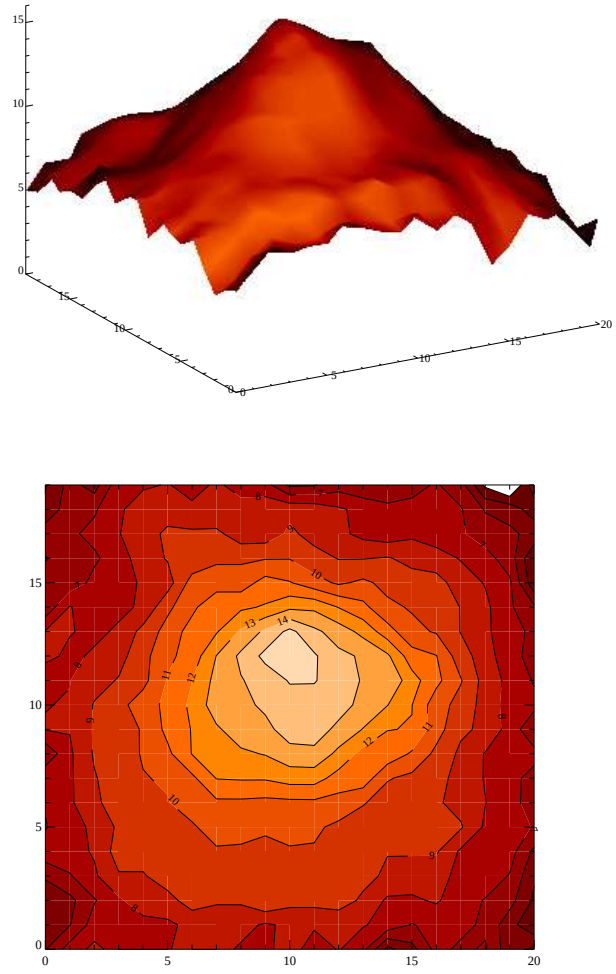

Figure 17: Medium Camera — Upper: The focal length variation shown as a 3-D surface map. The z-axis indicates the number of the column on the focus mask which produces the best focus. The detector area was sampled by 21×20 spots; Lower: The contour map constructed from the upper 3-D map. Both figures were smoothed by a 2×2 median filter.

9.3 Wide Camera

The wide camera shows a focal length variation which is similar to but slightly larger than that of the narrow camera. The highest focus value is 10–11 while the lowest is 5–6. The focus change is again smooth and nearly circularly symmetric, but the center of symmetry is significantly diplaced from the field center toward upper left.

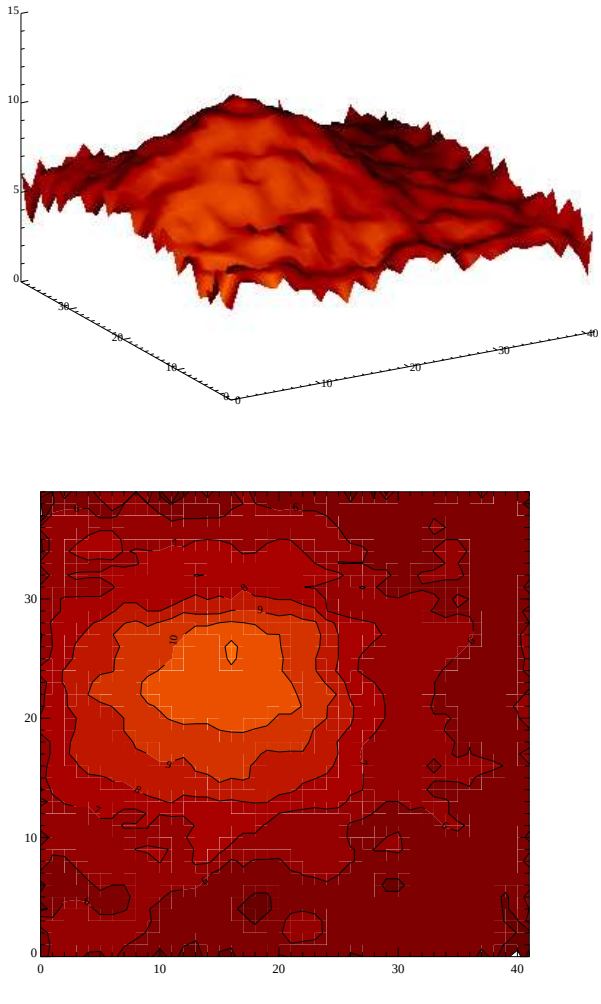

Figure 18: Wide Camera — Upper: The focal length variation shown as a 3-D surface map. The z-axis indicates the number of the column on the focus mask which produces the best focus. The detector area was sampled by 42×40 spots; Lower: The contour map constructed from the upper 3-D map. Both figures were smoothed by a 2×2 median filter.

Tests performed by E. Egami.

10 Geometrical Distortion

Purpose: In general, an optical system suffers from a variety of aberrations which either blur the image and affect the image quality (spherical aberration, coma, astigmatism) or move the image and affect the image position (field curvature, geometrical distortion). Since it is difficult to decouple these various types of aberrations and evaluate them seperately, we categorize our NIRC2 optics testing into two areas: geometrical distortion and image quality. Here, we first characterize the geometrical distortion (i.e., image displacement). The image quality will be discussed in the next section. A good understanding of geometrical distortion is important not only for astrometry but also for photometry since a severe distortion could cause pixels to have different effective areas as a funciton of position.

Distortion Masks: The distortion mask has two rectangular grids of holes. The larger grid has 43×43 8 μm of diameter holes with a 7mm separation while the smaller grid has 21×21 of 4 μm diameter holes with a 3.5mm separation. The former grid is used with the Medium and Wide cameras while the latter is used used with the Narrow camera. These grids are made very precisely so that the deviations of the hole images from the known grid patterns allow us to measure the direction and magnitude of distortion.

Procedure: A pair of images were taken for each camera with the distortion mask in. Between two exposures, the mask was moved by half the hole separation so that a background-subtracted image can be obtained from the two. The J, Ks, and Ms filters were used with integration times of 1800s, 180s, and 1s, for the Narrow, Medium, and Wide cameras, respectively. The spot positions were measured for grids of 21×19, 21×20, and 41×41 for the Narrow, Medium, and Wide cameras, respectively. Since the grid axis is slightly rotated with respect to the rows and columns of the detector, the measured spot positions were first rotated by 0.44deg, 0.52deg, and 0.34deg in the counter-clockwise direction for the Narrow, Medium, and Wide cameras, to offset this misalignment.

Results: The rotated spot positions were compared with those expected from the mask grid pattern. The distortion pattern was fit by the following cubic polynomial:

$$\begin{aligned} x\prime &= a_0 + a_1 x + a_2 y + a_3 x^2 + a_4 xy + a_5 y^2 \\ &\quad a_6 x^3 + a_7 x^2 y + a_8 x y^2 + a_9 y^3 \end{aligned}$$

$$\begin{aligned} y\prime &= b_0 + b_1 x + b_2 y + b_3 x^2 + b_4 xy + b_5 y^2 \\ &\quad b_6 x^3 + b_7 x^2 y + b_8 x y^2 + b_9 y^3 \end{aligned}$$

$$\begin{aligned} x &= x_{obs} - 512 \\ y &= y_{obs} - 512 \end{aligned}$$

where (x_{obs},y_{obs}) is the measured spot position, ($x\prime$, $y\prime$) are the distortion corrected position, and a_i and b_i are the polynomical coefficients. The distorion was defined to be zero at the center of the array (512, 512), and the coefficients were determined by substituting the distortion-free spot positions (x_0, y_0) (i.e., the known grid pattern of the distorion mask) into ($x\prime$, $y\prime$). The results are listed in the table below:

Camera	Narrow	Medium	Wide
a_0	(-2.72 ± 0.94)E$-$01	(-3.1253 ± 0.0049) E$-$01	(4.06 ± 0.46) E$-$01
a_1	(1.0009 ± 0.0005)E+00	(9.99382 ± 0.00002) E$-$01	(1.0008 ± 0.0002) E+00
a_2	(5.08 ± 0.52)E$-$03	(1.2397 ± 0.0017) E$-$03	(-3.24 ± 0.23) E$-$03
a_3	(-5.52 ± 0.52)E$-$06	(-2.8046 ± 0.0042) E$-$06	(-1.75 ± 0.33) E$-$06
a_4	(7.7 ± 6.4)E$-$07	(1.2002 ± 0.0058) E$-$06	(-5.6 ± 3.0) E$-$07
a_5	(5.37 ± 0.80)E$-$06	(1.0880 ± 0.0005) E$-$05	(10.00 ± 0.33) E$-$06
a_6	(-8.6 ± 2.6)E$-$09	(-9.6170 ± 0.0098) E$-$09	(-6.8 ± 1.3) E$-$09
a_7	(-8 ± 25)E$-$10	(-1.514 ± 0.015) E$-$09	(8 ± 12) E$-$10
a_8	(-6.1 ± 2.7)E$-$09	(-5.053 ± 0.016) E$-$09	(-3.6 ± 1.2) E$-$09
a_9	(-4.4 ± 3.4)E$-$09	(3.90 ± 0.11) E$-$10	(9 ± 13) E$-$10
b_0	(1.68 ± 0.94)E$-$01	(3.87 ± 0.92) E$-$01	(3.4 ± 4.6) E$-$02
b_1	(1.6 ± 4.7)E$-$04	(-1.4 ± 4.6) E$-$04	(2.1 ± 2.3) E$-$04
b_2	(1.0008 ± 0.0005)E+00	(9.9573 ± 0.0048) E$-$01	(9.9477 ± 0.0023) E$-$01
b_3	(2.1 ± 6.5)E$-$07	(7.6 ± 6.4) E$-$07	(-4.4 ± 3.3) E$-$07
b_4	(-9.93 ± 0.64)E$-$06	(-8.27 ± 0.60) E$-$06	(-9.2 ± 3.0) E$-$07
b_5	(1.78 ± 0.80)E$-$06	(1.86 ± 0.72) E$-$06	(-1.57 ± 0.33) E$-$06
b_6	(-1.6 ± 2.6)E$-$09	(3 ± 25) E$-$10	(2 ± 13) E$-$10
b_7	(-2.8 ± 2.5)E$-$09	(-1.6 ± 2.3) E$-$09	(2.6 ± 1.2) E$-$09
b_8	(-4 ± 27)E$-$10	(8 ± 24) E$-$10	(5 ± 12) E$-$10
b_9	(-1.2 ± 0.35)E$-$08	(-6.4 ± 2.8) E$-$09	(5.9 ± 1.3) E$-$09
$\Delta(x - x_0)$	0.4 ± 1.6	-0.3 ± 1.2	-1.1 ± 1.3
$\Delta(y - y_0)$	-0.3 ± 1.14	-0.5 ± 1.7	0.1 ± 1.2
$\Delta(x\prime - x_0)$	$(-7.4\text{E}-7) \pm 0.81$	$(-2.6\text{E}-06) \pm 0.31$	$(-9.8\text{E}-06) \pm 0.57$
$\Delta(y\prime - y_0)$	$(1.1\text{E}-6) \pm 0.62$	$(-2.3\text{E}-09) \pm 0.34$	$(4.7\text{E}-08) \pm 0.29$

10.1 Narrow Camera

With the narrow camera, the central part of a few hundred pixels on a side is almost distortion free, but outside that region, the distortion increases toward the edges, where the image motion becomes 4–5 pixels. As can be seen below, the distortion is almost completely fitted out with the cubic polynomial with a 1σ residual of (0.81, 0.62) pixels.

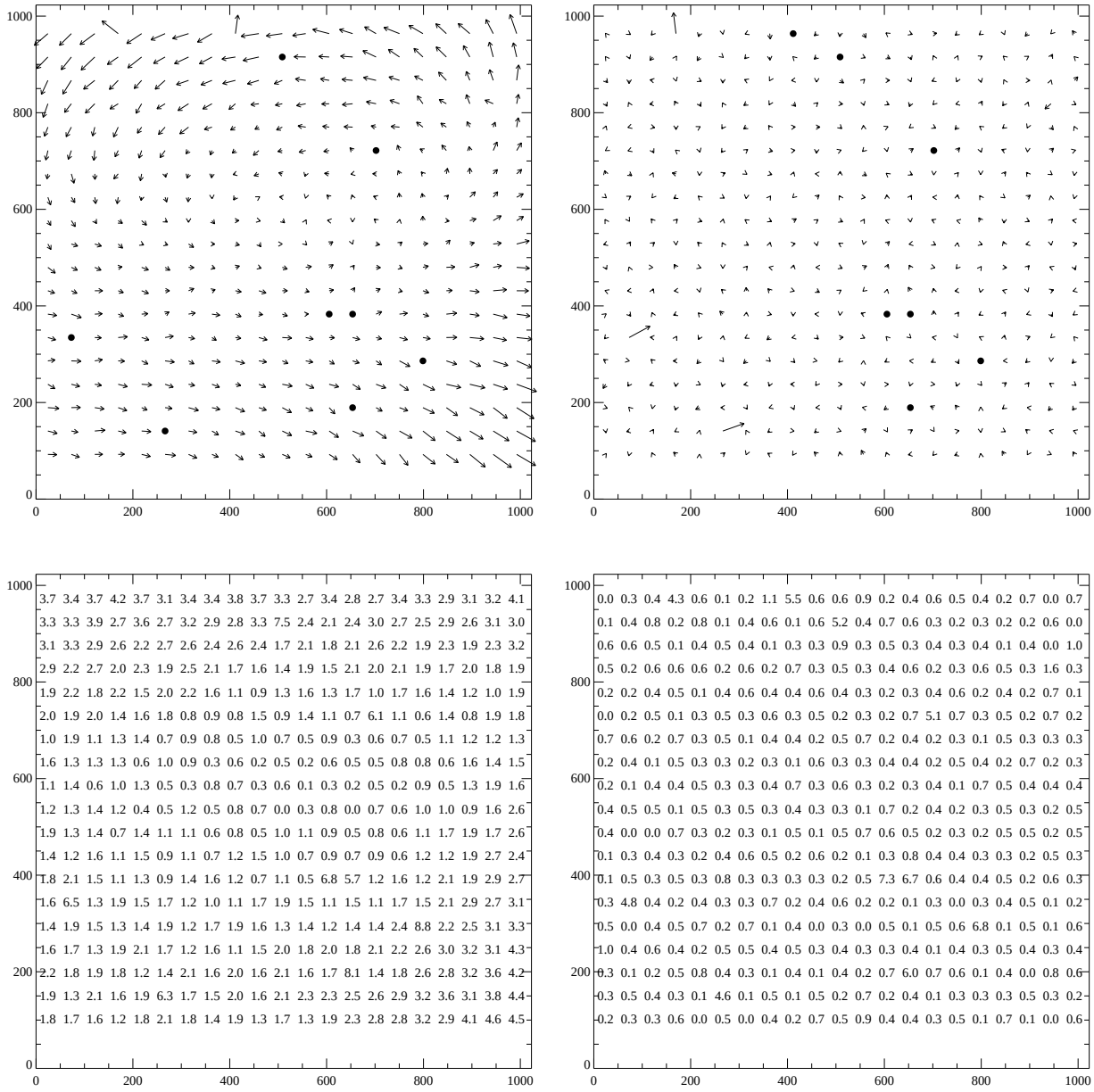

Figure 19: Narrow Camera — *Upper left*: The geometric distortion detected with the narrow camera. The direction and length of an arrow indicate the direction and magnitude of distortion at the position of the arrow's tail. The arrow length was set to 10 times that of the actual image motion in pixels. The filled circles indicate the positions of defective mask spots; *Lower left*: The actual size of the image motion in pixels (i.e., 1/10 of the arrow length); *Upper right*: The residual after the distortion correction; *Lower right*: The residual in pixels.

10.2 Medium Camera

With the medium camera, the overall distortion pattern is more or less axisymmetric with respect to the central row of the detector. The distortion is very little within 100–150 rows on the both side of the central row except for the region close to the right edge. The distortion increases as a function of distance from the central row, reaching 4–5 pixel image shifts near the lower and upper edges. The 1σ residual after the distortion correction is (0.31,0.34) pixels.

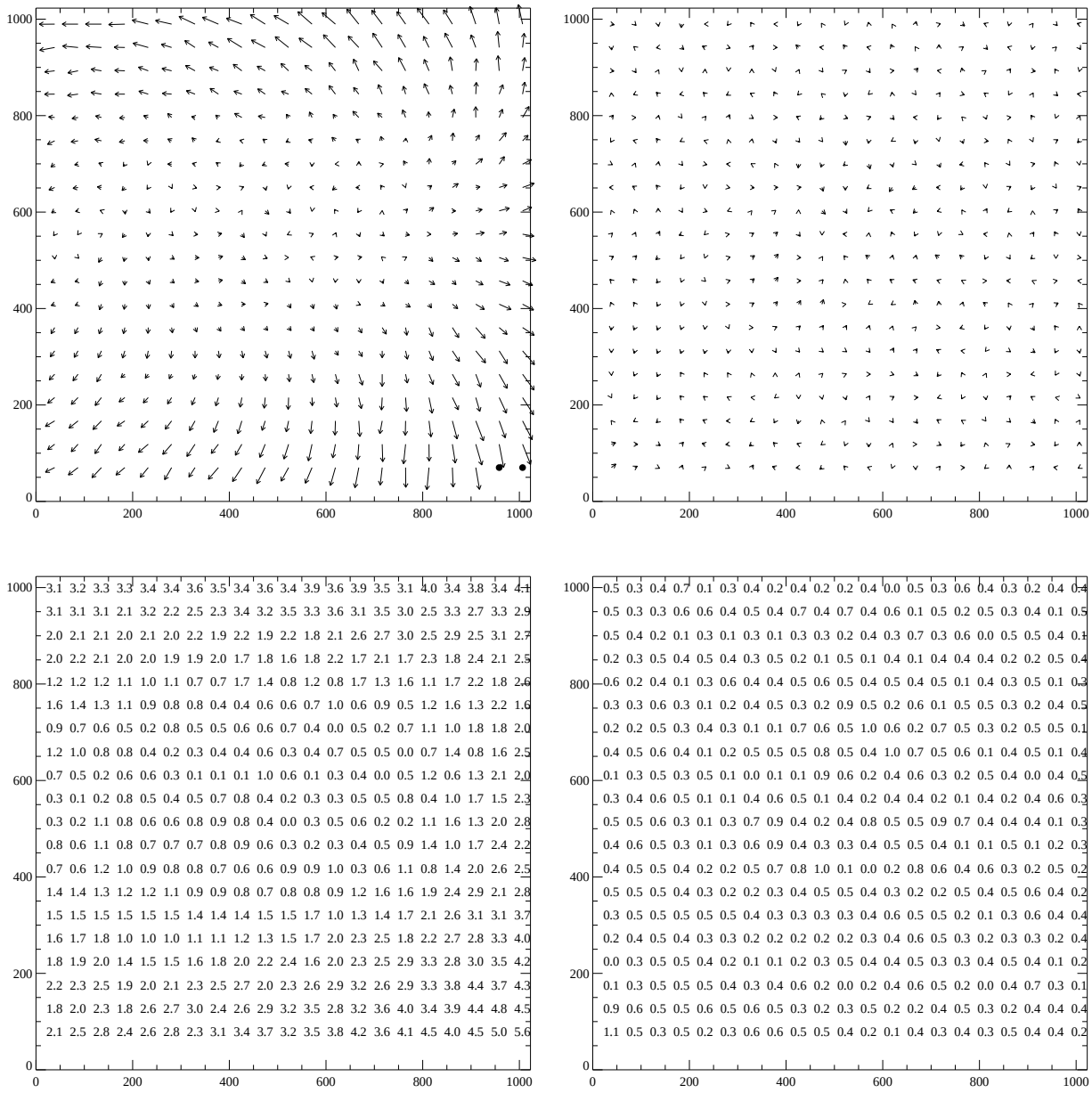

Figure 20: Medium Camera — *Upper left*: The geometric distortion detected with the medium camera. The direction and length of an arrow indicate the direction and magnitude of distortion at the position of the arrow's tail. The arrow length was set to 10 times that of the actual image motion in pixels. The filled circles indicate the positions of defective mask spots; *Lower left*: The actual size of the image motion in pixels (i.e., 1/10 of the arrow length); *Upper right*: The residual after the distortion correction; *Lower right*: The residual in pixels.

10.3 Wide Camera

The distortion pattern with the wide camera is also more or less axisymmetric with respect to the central row with the magnitude of distortion increasing as a function of distance from the central row. However, there also exists a noticeable difference between the lower and upper parts of the detector in the sense that the images in the lower part shift more toward left. The ∼100 rows on the both side of the central row suffer from very little distortion. The 1σ residual after the distortion correction is (0.57, 0.29) pixels.

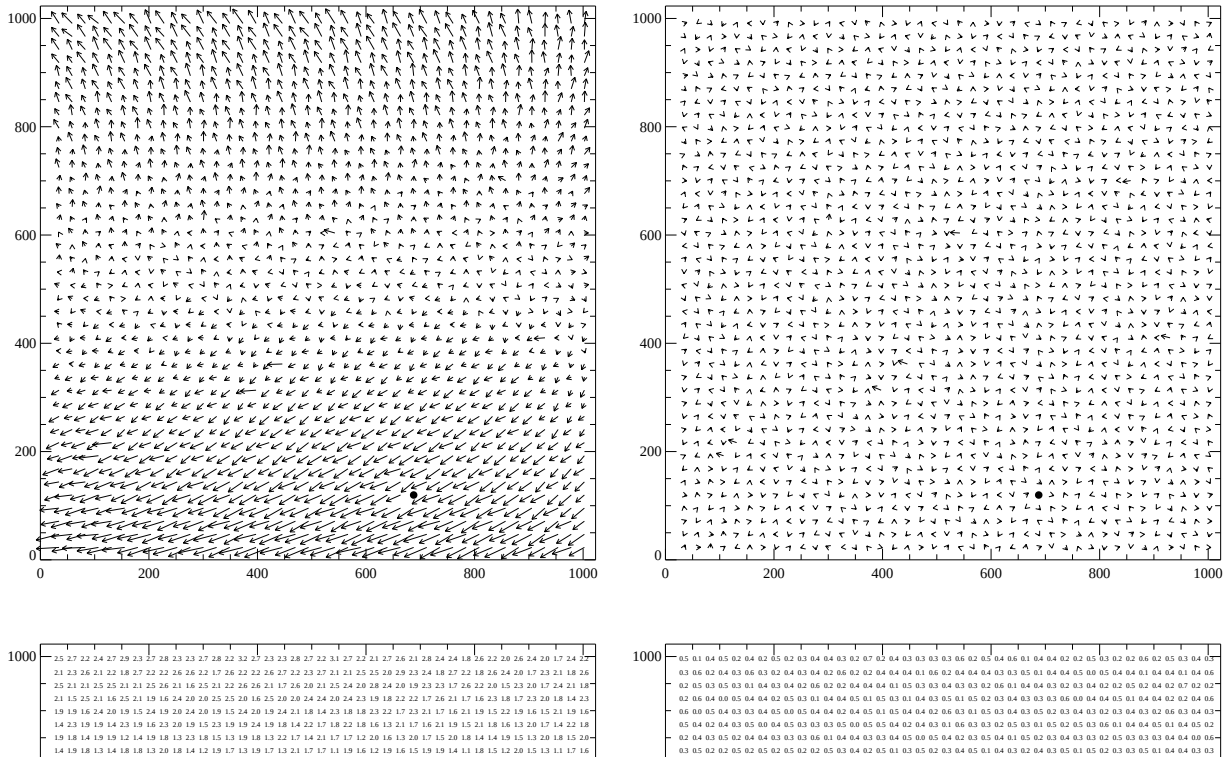

Figure 21: Wide Camera — *Upper left*: The geometric distortion detected with the wide camera. The direction and length of an arrow indicate the direction and magnitude of distortion at the position of the arrow's tail. The arrow length was set to 10 times that of the actual image motion in pixels. The filled circles indicate the positions of defective mask spots; *Lower left*: The actual size of the image motion in pixels (i.e., 1/10 of the arrow length); *Upper right*: The residual after the distortion correction; *Lower right*: The residual in pixels.

TESTS PERFORMED BY E. EGAMI.

11 Image Quality

Purpose: In this section, we examine the quality of the images produced by NIRC2. A significant degradation could result from various aberrations of the optics, and a good understanding of such effects will be crucial when trying to understand whether some features seen are produced by NIRC2, the AO system, or the object itself.
Procedure: For this test, we basically use the images taken for the geometric distortion test and examine the morphology and half-light radius of each individual spot. The details of the image acquisition can be found in the previous section.

Based on the light growth curve, we assume that an 8-pixel radius apeture can be used to measure the total light of each spot. The sky level was estimated within an annulus just outside this apeture. After the sky level was subtracted, the growth curve was constructed using eight cocentric circular apertures with radii of 1, 2, 3, 4, 5, 6, 7, and 8 pixels. This growth curve was then fitted with a cubic spline function, with which we estimate the radius of a circular aperture which contains half of the total counts. In the following, the results are described for each camera.

11.1 Narrow Camera

Figure 22 shows the half light radii of the spots produced by the distortion mask as a function of position on the detector.

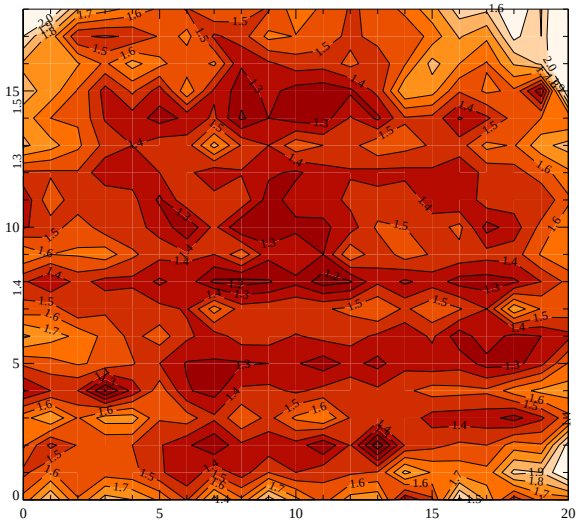

Figure 22: A contour map showing half-light radii of the spots. The image was taken with the J filter. The whole detector was covered by a square grid of 21 × 19 spots. The bright colors correspond to larger half-light radii.

As can be seen in the figure, the variation of the half-light radius over the detector area is not very large ($r_{1/2} = 1.2 - 1.5$ pixels) except for the regions close to the edges, where the half-light radius approaches 2 pixels near the corners. This degradation of the image quality is clearly seen in Figure 23 as the image elongation in the radial direction from the detector center.

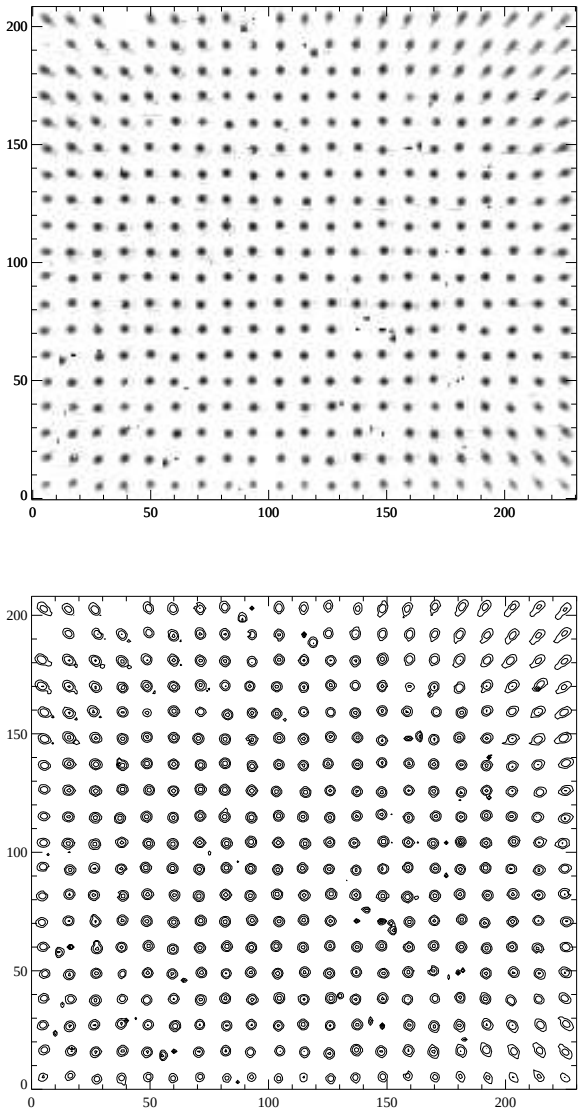

Figure 23: Upper: A log-scale image of the spots produced by the distortion mask. The 11 × 11 pixels centered on each spot is shown; Lower: The contour map of the top image. Each contour denotes a factor of 2.5 increase in the brightness;

11.2 Medium Camera

As expected from the severe curvature of the focal plane detected in the focus test, the medium camera shows the largest variation of the half-light radius. As Figure 24 shows, the half-light radius increases substantially (approaching 2 pixels) near the field center, where the focus test showed a significant deviation of the focal length from the nominal value. The increase of the image size near the field center is also seen clearly in Figure 25. For the rest of the detector area, the variation of the half-light radius is relatively small, ranging from 1.2 to 1.4 pixels.

The spot images near the detector edges look also severely distorted in the sense that they show a significant elongation in the radial direction from the field center. However, as can be seen in Figure 24, the half-light radii of these spots are not as large as those near the field center. This indicates that the image quality of these spots are not as bad as Figure 25 might suggest. These images have a sharp peak which contains most of the flux, and the image elongation is only visible at fainter level, which becomes more conspicuous in the log-scale image/contour in Figure 25.

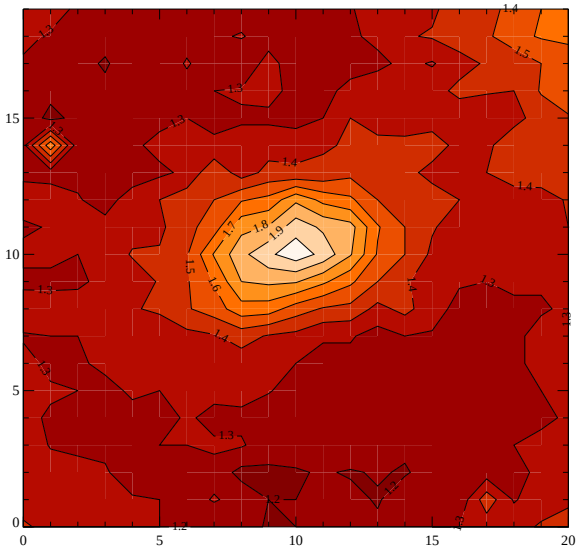

Figure 24: A contour map showing half-light radii of the spots. The image was taken with the Ks filter. The whole detector was covered by a square grid of 21 × 20 spots. The bright colors correspond to larger half-light radii.

These results indicate that with the medium camera, the image quality changes rather substantially over the field of view. This seem to imply that the useable detector area of the medium camera might be considerably smaller than those of the other two cameras in the sense that only the images in a limited region can be properly focused at one time.

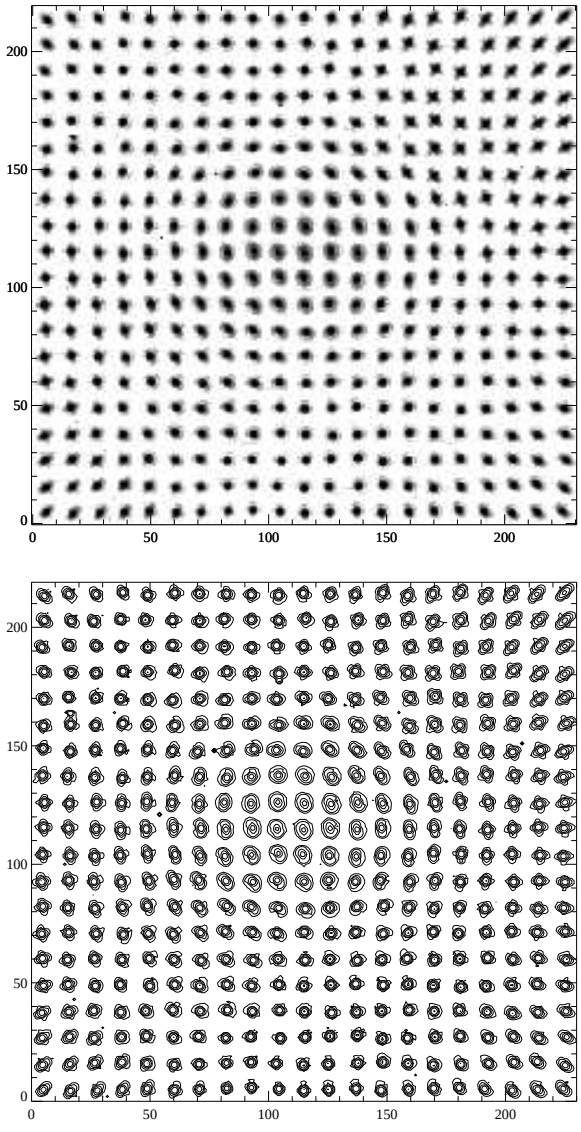

Figure 25: Upper: A log-scale image of the spots produced by the distortion mask. The 11×11 pixels centered on each spot is shown; Lower: The contour map of the top image. Each contour denotes a factor of 2.5 increase in the brightness;

11.3 Wide Camera

The wide camera shows the least variation of the image quality over the detector area as seen in Figure 26 and 27, Again, the images near the detector edges are elongated in the radial direction from the field center, but these image deformations are not large enough to severely changes the value of the half-light radii.

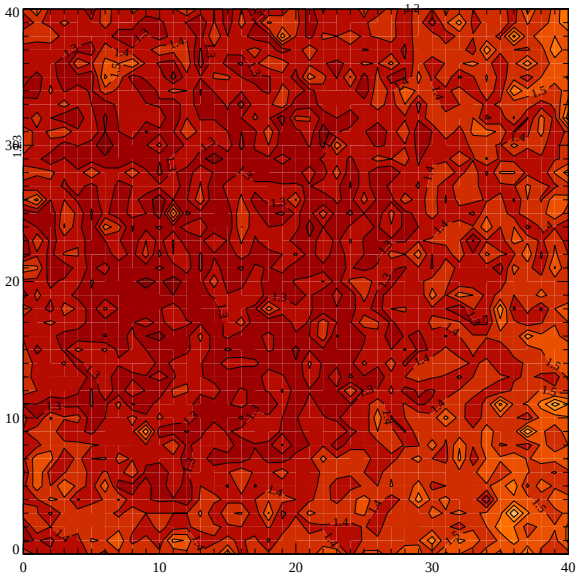

Figure 26: A contour map showing half-light radii of the spots. The image was taken with the *Ms* filter. The whole detector was covered by a square grid of 41 × 41 spots. The bright colors correspond to larger half-light radii.

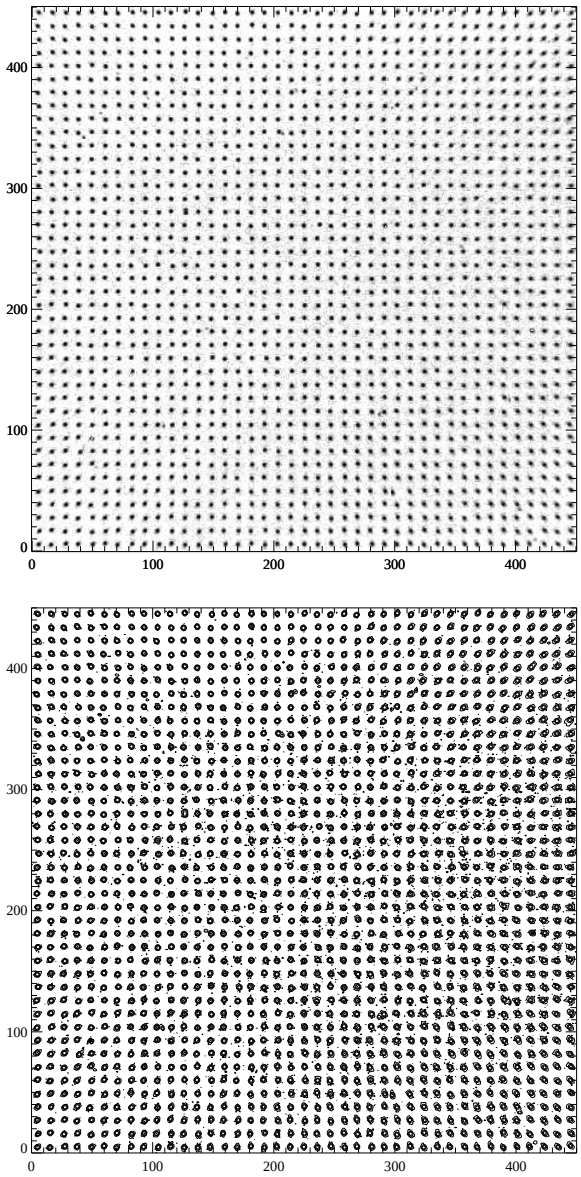

Figure 27: Upper: A log-scale image of the spots produced by the distortion mask. The 11×11 pixels centered on each spot is shown; Lower: The contour map of the top image. Each contour denotes a factor of 2.5 increase in the brightness;

TESTS PERFORMED BY E. EGAMI.

12 Pupil Lens

Tests in progress.

Tests performed by d. thompson.

13 Electrical Gain

The electrical gain is the proportionality constant used to convert the number of detected electrons into the analog-to-digital units (ADU; also data number, DN). From Poisson statistics, we have that the uncertainty in measuring N detected electrons is equal to the square root of N:

$$\sigma = N^{0.5}$$

However, we can only measure the signal (S) and uncertainty on S (σ_S) in terms of the recorded ADU. The signal is just the gain (g) times the number of detected electrons:

$$S = g \times N$$

while the uncertainty on S is just the gain times the square root of N:

$$\sigma_S = g \times N^{0.5}$$

Eliminating N from these two equations leaves us a relation between two measureable quantities:

$$\sigma_S^2 = g \times S$$

We obtained a series of images of a uniformly illuminated source (essentially flatfield images) with different exposure times such that the detected signal spanned the full detector well capacities. The instrumental gain was set at the default, 4, for these tests. Mean counts (DN) and the noise (σ_S) were extracted. We note that it was necessary to fit and remove 60 Hz pickup noise prior to determining σ_S for these data. Figure 13 plots the variance vs. the mean counts for these data.

We derived a linear fit (dashed line) to the data in the box (dotted line) to determine the slope. Only the data in the box were used because the read noise contributes significantly to σ_S for lower DN, while non-linearities in the array response and saturation affect values at higher DN.

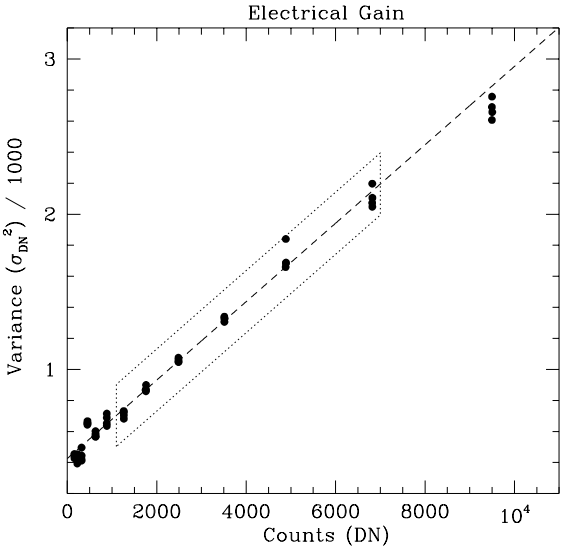

The slope of the fit to the boxed data is 0.2527, which is the electrical gain in units of DN/e$^-$. The inverse gain is thus 3.957 e$^-$/DN.

No tests were performed at other settings of the instrumental gain.

Tests performed by D. Thompson.

14 Offsets

Because the 16-bit A/D converters in the NIRC-2 electronics cover the range of 0 to $2^{16} - 1$, it is necessary to ensure that the electronics always sees a positive signal so that no data are lost. If the offsets were set to zero DN, then a dark frame with zero signal plus the uncertainties due to the read noise would produce negative signals, which would be truncated to zero when digitized. To circumvent this effect, electronic offsets are added to the raw signal from the array before the data reach the A/D converters.

There is potentially a similar effect if the signal exceeds the capacity of the A/Ds, so it is also important to not set the offsets too high. In practice, the dynamic range of the A/Ds is higher than the well depth of the detector divided by the gain (e^- per A/D units), so this is not a major concern.

It would be perfectly acceptable to run the instrument using the same offsets for all four quadrants. In double-correlated sampling mode (sampmode 2) or Fowler sampling mode (sampmode 3), these offsets are subtracted off before the data are saved to disk. However, slight differences in the four independent sets of electronics which read out the four quadrants result in small residual differences between the four quadrants. This can be seen in Figure 28, where the offsets have been set to a constant of 3150 and the array read out in single-correlated read mode (sampmode 1).

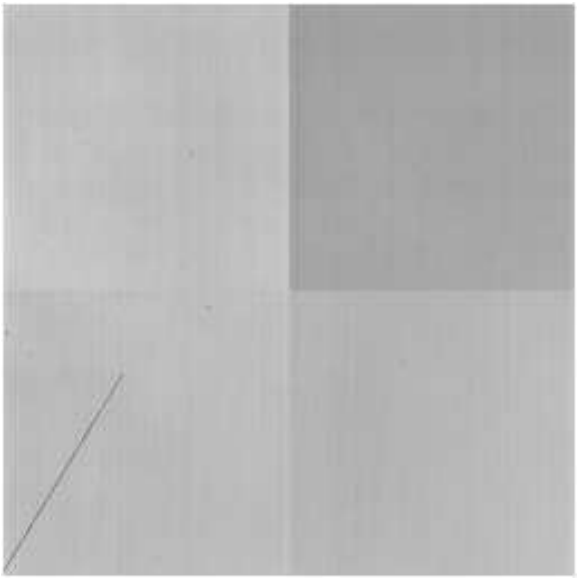

Figure 28: The NIRC-2 array read out in single-correlated read mode using a constant offset of 3150 for all four quadrants.

In order to determine the optimal offsets to use for each quadrtant, we first obtained a series of dark images with different constant offsets spanning the range of [3080,3200]. We then performed a least-squares fit to the value of the minimum pixel as a function of the offset. This determines an absolute minimum offset for each quadrant where the minimum pixel has a value of zero. This fit also yielded an offset calibration: a Δoffset of one produces a change in the bias level of 186.5 A/D units.

Next, the histograms of the pixel values in each quadrant were compared at a constant offset in order to determine the small differences in mean bias level between quadrants. Combining these with the absolute minimum offsets gives a minimum offset which will both keep all pixels at or above zero and match the mean levels in the four quadrant. Finally, we add a small constant (Δoffset = 10) to these values for the final recommended offsets. This will keep the minimum pixel safely above zero without exceeding the A/D dynamic range. These three sets of offsets (absolute minimum, minimum to match mean bias levels, and recommended default offsets) are given in Table 14. In Figure 29 we show a dark frame in single-correlated mode using the recommended offsets.

	Abs. Min.	Match Means	Safest Offsets	Best Offsets
Q1	3162	3162	3172	3124
Q2	3134	3173	3183	3135
Q3	3162	3170	3180	3132
Q4	3137	3173	3183	3135

There are only three pixels which would be lost by setting the offsets lower by 48, to 3124 3135 2132 3135. The three bad pixels are at locations (669,293), (872,777) and (872,778) on the array (IRAF coordinates number from 1).

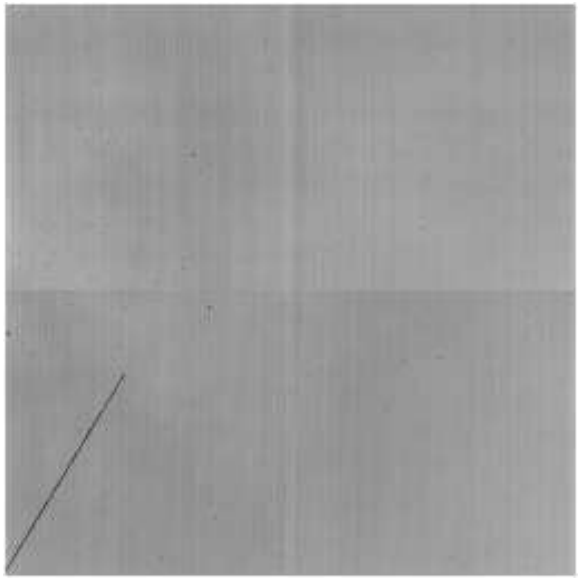

Figure 29: The NIRC-2 array read out in single-correlated read mode using the recommended offsets for each quadrant.

They do not appear to be bad pixels (hot or dead).

We also tested that these offsets work for subframing as well as with different pixel sampling rates. In all cases, they appear to be OK. No tests were done with a amplifier gains other than the default value.

Tests performed by D. Thompson.

15 Pickup Noise

Noise from sources outside of the array itself is known as pickup noise. This can come from crosstalk between adjacent wires, dirty power supplies, or a number of other sources. Proper shielding may eliminate some of this pickup noise, but it is difficult to eliminate it entirely.

Given that NIRC-2 will be moved from the lab here at Caltech to the Keck-II telescope, only cursory testing of the pickup noise was performed. More extensive testing, including identification and, to the extent possible, elimination of noise sources will be performed when NIRC-2 is installed in the dome on Mauna Kea.

To check for pickup noise, we obtained four series of 100 dark frames obtained in single read mode (sampmode 1). The four sets of 100 were separated in time by 1 hour breaks to check for longer-term stability of the noise sources. Each set of 100 images were also averaged and then subtracted from the individual exposures to check for short-term variations in the pickup noise.

The primary source of noise appears to come from the AC line current at 60 Hz (Figure 30). The 60 Hz pickup noise appears as broad horizontal striping with a period of ∼62.8 rows. The amplitude can be high; in Figure 30 it reaches to ∼20 DN peak-to-peak in the example shown, similar in magnitude to the read noise.

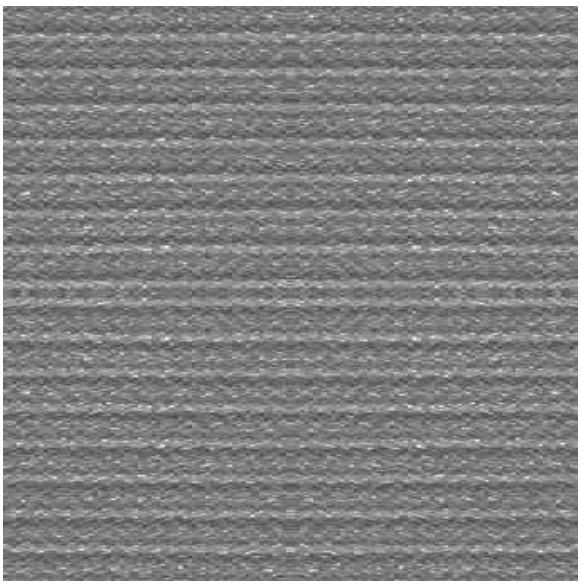

Figure 30: Pickup from 60 Hz line voltage. This is the most common form of pickup noise seen in the NIRC-2 data so far. The full array is shown in all figures in this section for reference.

Often seen in double-correlated sampling data (sampmode 2), especially darks, is the diamond shaped pattern shown in Figure 31. Fourier analysis gives a frequency near 6.2 KHz for this pickup noise. The source is unknown. There are some timing issues to resolve in the readout of the array, so this is only a preliminary result.

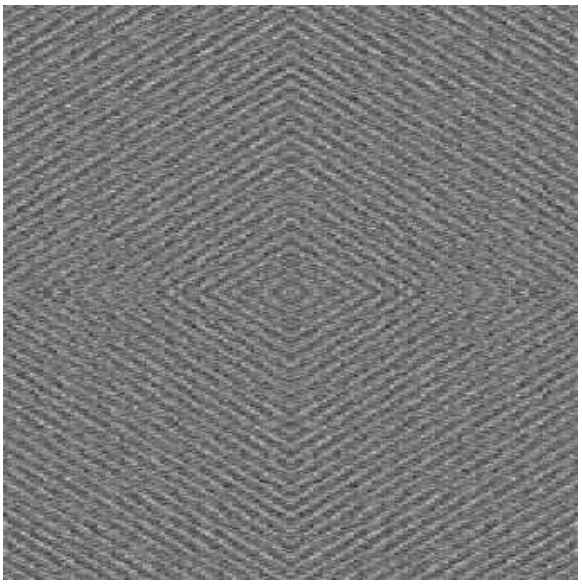

Figure 31: This pattern of pickup noise is also fairly common.

We show two other patterns of pickup noise in Figures 32 and 33 seen during testing of NIRC2. The source of the noise shown in these figures is unknown. The fourier analysis yields odd frequencies of ≃155 Hz and near 60 Hz.

Tests performed by D. Thompson.

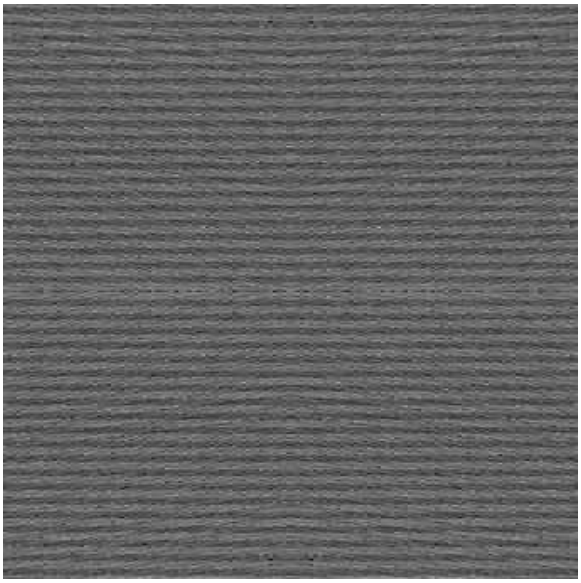

Figure 32: A high-frequency horizontal striping is less common. Its source is unknown. Fourier analysis suggests that this is primarily from a noise source with the odd frequency of $\simeq$155 Hz.

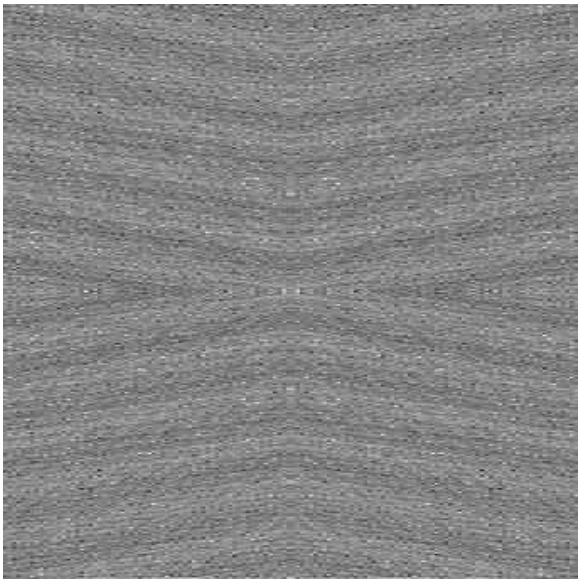

Figure 33: This low-frequency chevron pattern is less common. Its source is unknown, with a fundamental frequency near 60 Hz.

16 Subframing

All allowable subframe modes have been tested and all work. A partial list is given in Table 16, which are the modes listed by the NIRSPEC gui. The complete list is considerably more extensive and are not listed here. Note that only centered subarrays are allowed.

All modes work at the default pixel sample rate (SAMPRATE = 250 kpix/s). A subset of these modes were tested at a range of pixel sample rates spanning the currently allowed range.

Nx	Ny				
1024	1024	768	512	256	128
	64	32	16	8	
768	1016	760	504	248	120
	56	24	8		
512	1024	768	512	256	128
	64	32	16	8	
256	1016	760	504	248	120
	56	24	8		
128	1016	760	504	248	120
	56	24			
64	1016	760	504	248	120
	56				
32	1016	760	504	248	120

The allowed subframe modes must follow these three rules:

1. The number of columns (Nx) in the subframe must be divisible by 32.
2. The number of rows (Ny) in the subframe must be divisible by 8.
3. Nx*(Ny+8) must be divisible by 4096.

The only caution to note is that for some of the modes which are taller than they are wide, there is an aliasing in the display GUI where large blocks of rows alternate between odd and even numbered rows (Figure 34). Because there is a small offset between odd and even rows due to the architecture of the array, the display shows strong horizontal striping. This is purely an effect of the quicklook display GUI and **not** in the data. This effect shows in all sample modes. Zoomed displays do not show this effect even when the full displayed image does.

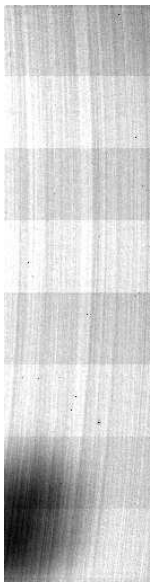

Figure 34: Example of the display aliasing when in subframe modes, here 256×1016 pixels. This is seen primarily when the image is taller then wide (Nx<Ny) and the Ny dimension not a power of two.

TESTS BY D. THOMPSON, B. GOODRICH.

17 Camera Stage

The camera stage in NIRC2 carries three different imaging cameras: the WIDE , MEDIUM , and NARROW cameras. The image scale is approximately 40, 20, and 10 mas per pixel, repsectively. These pixel scales allow for slightly better than Nyquist sampling at 4.0, 2.0, and 1.0 μm.

Note that the placement of the cameras on the stage, with the NARROW camera in the middle, was chosen to minimize the length of the stage as well as equalize the offsets between cameras. Thus, movement to the WIDE or MEDIUM cameras always comes from the same direction, while movement to the NARROW camera can be from both directions.

17.1 Calibration

Initially, we calibrated the camera stage relative to motor position with respect to the smallest coronographic spot. Subsequent inconsistencies, such as vignetting from other mechanisms in the WIDE and MEDIUM cameras, suggested a problem with the absolute position of the spot mask in the direction which is parallel to motion of the camera stage. We therefore recalibrated the camera stage using the imaging apertures in the slit mask stage (SLM). These positions for the cameras gave internally consistent results and eliminated the vignetting seen in earlier work. The motor counts for proper camera alignment are given in the table below.

Camera Position

Camera	Motor Cts.
WIDE	35848
MEDIUM	427041
NARROW	260606

17.2 Reproducibility

To test the reproducibility of the camera stage mechanism, we obtained images of the distortion mask over 10 cycles up and down the length of the stage. Centroids on the many spot images (of order 400 for the WIDE and MEDIUM cameras and 100 for the NARROW camera) were used to reduce the uncertainties on the mean relative positions of the cameras. The initial test was done with the motor backlash parameter set to +200 counts. While the WIDE and MEDIUM cameras showed excellent reproducibility, the NARROW camera showed a difference of $\sim$2 pixels depending on if the last move came from the direction of the WIDE camera or the MEDIUM camera.

To check that this 2-pixel offset was not simply due to a backlash problem in the stage drive, we repeated the 10-cycle test with the motor backlash parameter set to +2000 as well as -2100, corresponding to a full turn of the motor shaft. The results of these tests are shown in Figure 35. In all of the plots, the solid circles represent the residual vertical offsets (relative to the first image in each set), which is parallel to the motion of the camera stage. The crosses mark the residual horizontal offsets, which are perpendicular to the direction of the camera stage motion. The uncertainties are plotted as short vertical lines on each data point, and span the 25th percentile and 75th percentile points in the distribution of the centroids. For many of the plotted points, these error bars are smaller than the size of the point itself.

The WIDE camera (top two plots in Figure 35) shows an rms reproducibility of 0.08 pixels for the test with backlash set to +2000. The uncertainty is slightly lower in the negative backlash test.

The MEDIUM camera (middle two plots in Figure 35) shows an rms reproducibility of 0.03 pixels for the first test (left plot). The uncertainty is slightly higher in the negative backlash test, opposite in sense to the WIDE camera results.

The NARROW camera (bottom two plots in Figure 35) shows an rms reproducibility of 0.14 pixels in each set of data with a consistent approach direction, but a two pixel offset between the two sets of data. The exact source of this offset is not clear. Note that the direction of this offset is along the length of the slits, so it should have little impact on imaging or spectroscopic science observations.

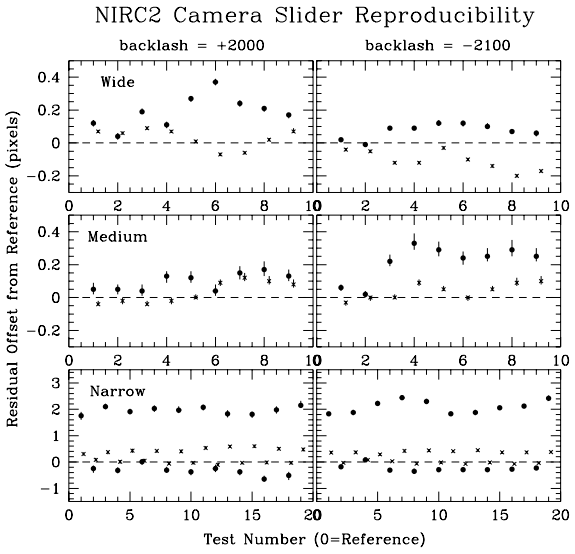

Figure 35: Repeatability of the camera stage mechanism. The solid circles plot the vertical residuals while the crosses plot the horizontal residuals (offset by Δx=0.2). The error bars span the 25th to 75th percentiles on the distribution of centroids at each point.

We note that additional testing of the narrow camera using move-motor commands to offset the stage $\pm$20,000 motor counts (about 10% of the distance to the WIDE and MEDIUM cameras) from the nominal position produced similar results. Therefore the backlash parameter was reset to +200 motor counts, consistent with the other mechanisms in NIRC2. However, for the most accurate positioning we recommend that moves from the MEDIUM camera to the NARROW camera go through the WIDE camera position first. This is how all subsequent testing and calibration of NIRC2 using the NARROW camera was done.

TESTS PERFORMED BY D. THOMPSON.

18 Grism Stage

Tests in progress.

Tests performed by D. Thompson.

19 The Shutter

The shutter is a simple rotating blade. It is located between the grism stage and the filter wheels.

19.1 Performance

To test how well the shutter (and baffles) blocks light, we configured NIRC2 for wide-field imaging, which will allow the largest amount of light to enter the dewar. We then obtained two 600 s images through the J band filter, and another two 600 s images through the M_s filter. Fowler sampling (N = 32) was used to reduce the read noise. The amount of J band light available is affected by room lights and continuum lamps, but the M_s band is completely dominated by thermal emission from the room itself.

Since there are far more photons at 5 microns than at 1.25 microns, any excess signal in the $M_s - J$ difference images should come from scattered long-wavelength photons which make it past the shutter. The photons reaching the array which originate outside the dewar must undergo multiple reflections off various surfaces within NIRC2, as the system is well baffled.

There is a marginal excess signal in the M_s images over the J images, about 3 DN or 12 e^-. However, this is comparable to the quadrant to quadrant variations in the mean levels. The shutter and baffling in NIRC2 *do* effectively block essentially all light from reaching the array. Since an 0.25 s image saturates at M_s, we estimate the blocking to be $> 10^{-7}$ (at least 4×10^{-4} from the exposure time and 1.5×10^{-4} for the dynamic range of the detector).

19.2 Reliability

No failures of the shutter mechanism occurred during testing of NIRC2.

19.3 Calibration

No specific calibration of the shutter was done, as the initial values for the motor counts when opened (72) or closed (0) appear to be adequate.

Tests performed by D. Thompson.

20 Filter Wheels

20.1 Current Filters

NIRC2 is equipped with two filter wheels, each of which has 18 positions. Reserving one position in each wheel for an open hole, there are 34 positions available for filters. The current complement of filters in NIRC2, as of 10 April 2001, are given in Table 20.1.

Filter List

Pos	Inner Wheel	Outer Wheel
1	J	
2	H	
3		
4		H_{cont}
5		Fe II
6	K_s	
7	K'	
8		Brγ
9	K	
10		K_{cont}
11		
12	$PK50$ (1.5 mm)	
13		
14		
15	L'	$PK50$ (1.5 mm)
16	M_s	$PK50$ (1.0 mm)
17	OPEN	OPEN
18		

Tests performed by D. Thompson.

21 Pupil Mask

21.1 Rotation eccentricity

The rotating pupil masks are used to block out thermal radiation from the telescope and are designed to rotate so as to track these warm telescope components. The purpose of this test is to determine how much the rotating pupil masks wander as they are rotated.

The test was performed by taking images, spaced every 60deg apart, as each of the pupil masks was rotated. All four rotating pupil masks were followed for two full rotations and one (pup1rot) was followed for 2.5 rotations in one direction and 2.5 rotations in the reverse direction to check for any effects associated with backlash etc. At each angle, the centre of the pupil mask was located by constructing three lines joining the three sets of opposing spiders, and then determining the point of intersection of these three lines. This procedure locates the centre of the pupil mask on the image to $\sim \frac{1}{4}$ pixel.

Figure 21.1 shows the centres of the rotating pupil masks at different rotation angles. Rotating pupil masks 2 ("small inscribed hex") and 4 ("large inscribed hex") appear to wander by approximately 1.5 pixels edge-to-edge, while pupil masks 1 ("circumscribed circular") and 3 ("medium inscribed hex") wander by 4 and 5 pixels, respectively. One metre on the primary corresponds to 141 pixels, so on the primary, the side-to-side wander is approximately 1cm for masks 2 and 4, and 2.8–3.6 cm for masks 1 and 3.

The centres of the pupil masks at a given rotation angle appear to reproduce to better than $\frac{1}{3}$ pixel (or 0.25cm on the primary) over a full rotation (360 degrees) and there does not appear to be any effect associated with changing the direction of rotation.

The offsets between the centres of rotation of the four pupil masks can be made to be less than 2.5 pixels, or $\sim$ 1.8cm on the primary, if the PMS motor is set to positions 111583, 132419 , 161585, and 182418, for masks 1,2,3, and 4, respectively.

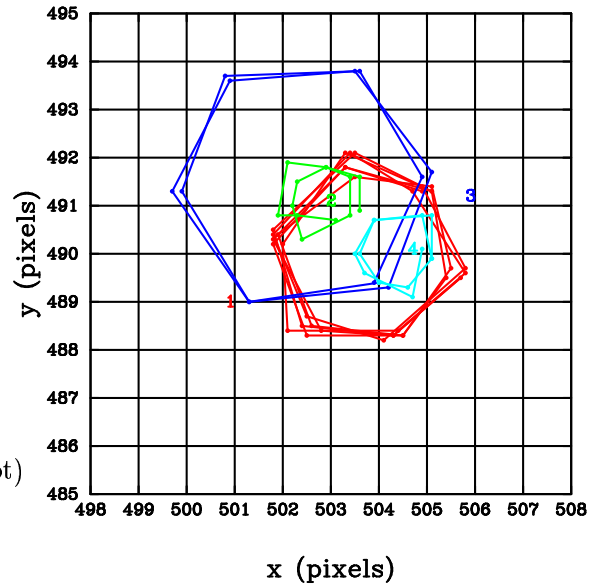

Movement of the centres of the four rotating pupil masks as the masks are rotated. The lines join mask centres determined for positions spaced 60 deg apart. A mask with no rotation eccentricity would show as a single point in this diagram. One pixel on the detector corresponds to $\sim$ 0.71cm on the primary

Tests performed by M. Sawicki.

22 Focal Plane Stage

The focal plane stage contains a slit mask which has 8 slits on it, spanning the range of 0.0073–0.1160 mm width, or 10–160 mas. There is also a coronagraphic spot mask which has ten spots spanning the range of 0.0725–1.4501 mm diameter, or 0.″1–2.″0. Both masks are made of vacuum deposited Inconel metal on a sapphire substrate. They are then supposed to be anti-reflection coated on both sides.

22.1 Reproducibility

The focal plane slider contains the spectroscopic slits and coronagraphic spots. With extremely narrow slits (10–160 mas) and small spots (0.1–2.0″) is important that the observer is able to reliably and reproducibly position the focal plane masks over objects in the field.

To determine the reproducibility of the focal plane slider (SLS stage), we obtained images of the edge of the imaging aperture, a slit, a coronagraphic spot, and the distortion mask over ten full cycles up and down the length of the stage. We used the NARROW camera, as this has the highest sensitivity to positions in the focal plane. Including the reference images, we have 22 measurements of the slits and spots, and 11 of the distortion mask.

In Figure 36 we plot the median offsets between the individual images and the reference (first) image. For the slits, the position was determined by averaging detector rows 510–515 and fitting a Gaussian profile to the slit image. The coronagraphic spots and distortion mask positions were found by centroiding on multiple peaks in each image.

Note that there is a marked slope to the data, most easily seen in the slit plot at the top of Figure 36. It is possible that cycling down the length of the SLS stage caused some local heating and expansion; the sign of the slope is correct for this explanation. The ten cycles over the full length of the SLS stage took place over ∼1 hr, far more than should be encountered under normal observing conditions, so this should not be a problem. However, to check that this was not a systematic problem in the SLS stage positioning, we repeated a single cycle up and down the length of the SLS slider >24 hours after the original measurements. These measurements, plotted to the right of the vertical dashed line in each panel, indicate that the SLS stage returned to a position coincident with the reference image to within the measurement uncertainty.

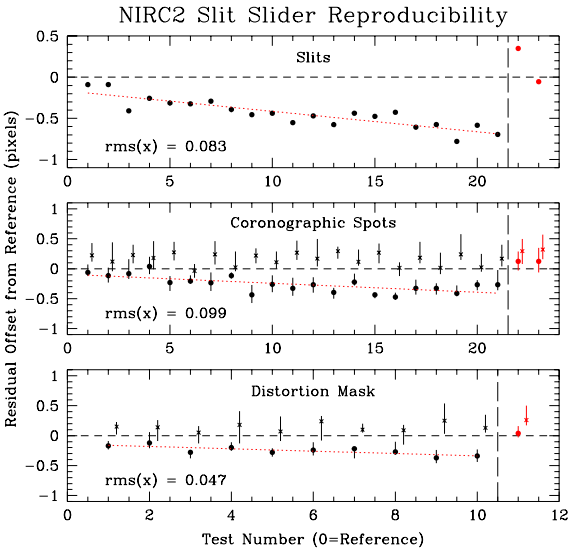

Figure 36: SLS stage reproducibility. Measurements for the slits, spots, and distortion mask are shown. The dotted lines indicate a first order fit to the data, from which the rms of the residuals is derived. The points to the right of the vertical dashed lines were obtained >24 hours after the main tests.

Given that there may have been some heating of the stage, we did a first order polynomial fit to the data to determine the reproducibility of the SLS stage. We find an rms on the residuals to the fit which is below a tenth of a pixel *in the* NARROW *camera*. The reproducibility in the MEDIUM and WIDE cameras should be smaller than this by factors of 2 and 4, respectively.

22.2 Calibration

22.2.1 Coronagraphic Spots

We obtained images with each of the ten coronagraphic spots at ∼10 positions across the array using the wide field camera. A scale drawing of

the spot mask is shown in Figure 37. The fits to the spot centroids vs. motor counts data allow derivation of the absolute motor counts required to place a spot at the requested column number. The calibrations fit the functional form of:

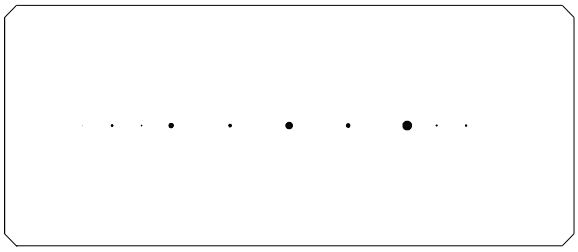

Figure 37: The coronagraphic spot mask. The ten spots project to 0.″1–2.″0 diameter on the sky.

$$motor\,\# = a_0 + a_1(col\,\#)$$

with the a_0 and a_1 parameters given in Table 22.2.1. The row number on which a given spot falls is essentially constant, varying by about 0.5 pixels from one end of the detector to the other. We include this constant row number in Table 22.2.1 as well. It represents a mean of the measured values and is appropriate for when the spot is near the center of the array.

Coronagraphic Spots - WIDE

D_{spot} (mm)	a_0	a_1	y_{cen}
0.0725	182872.0	-57.93713	484.45
0.2901	192897.3	-57.94081	485.93
0.1088	202885.8	-57.91982	487.03
0.7252	212941.6	-57.95980	488.90
0.4351	232941.0	-57.91727	491.55
1.0878	252971.8	-57.92295	494.36
0.5802	272990.0	-57.94602	497.00
1.4504	293029.5	-57.95180	499.70
0.1450	302973.0	-57.87557	500.62
0.2176	312994.8	-57.86593	501.93

Calibrations of the coronagraphic spots in the MEDIUM and NARROW cameras remain to be done.

22.2.2 Spectroscopic Slits

As with the coronagraphic spots, we obtained images of the eight slits at 11 positions across the array using the wide field camera. A drawing of the layout of the slit mask is shown in Figure 38. A linear fit to the data allow derivation of the absolute motor counts required to place a slit at the requested column number. The calibrations fit the functional form of:

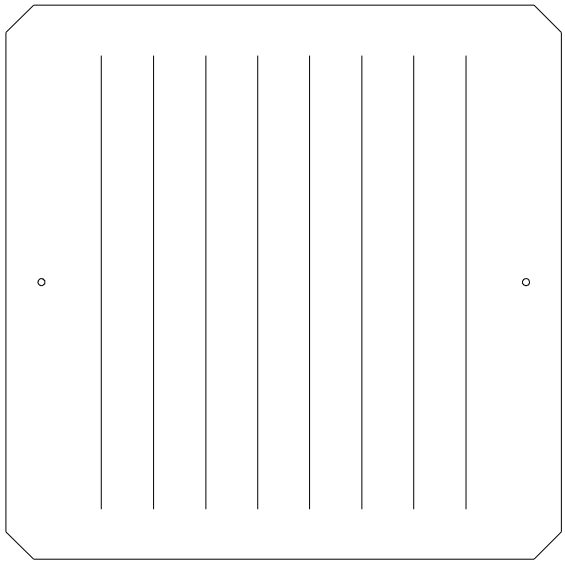

Figure 38: The slit mask. The eight slits project to 10–160 mas on the sky.

$$motor\,\# = a_0 + a_1(col\,\#)$$

with the a_0 and a_1 parameters given in Table 22.2.2.

Spectroscopic Slits - WIDE

Slit Width (mm)	a_0	a_1
0.0725	380465.9	-57.94318
0.	388101.4	-57.96233
0.	395728.2	-57.95171
0.	403348.4	-57.92937
0.	410984.2	-57.94677
0.	418607.4	-57.93188
0.	426232.4	-57.91983
0.1160	433824.1	-57.85712

TESTS PERFORMED BY D. THOMPSON.

23 Slit Mask Stage

Tests in progress.

Tests performed by D. Thompson.

24 Preslit Stages

Tests in progress.

Tests performed by d. thompson.